Saettone, S., Molinelli Fernandez, E., Soriano Gómez, C., Saavedra Ynocente, L. A., Duque Campayo, D., Souto-Iglesias, A., & Maron Loureiro, A. (2022). A particle image velocimetry investigation of the flow field close to a heave plate for models of different scales. Applied Ocean Research, 129, 103387. https://doi.org/10.1016/j.apor.2022.103387

A Particle Image Velocimetry Investigation of the Flow Field Close to a Heave Plate for Models of Different Scales

Simone Saettone[a], Enrique Molinelli Fernandez[b], Cristina Soriano Gómez[b], Leandro Antonio Saavedra Ynocente[b], Daniel Duque Campayo[c], Antonio Souto-Iglesias[d], and Adolfo Maron Loureiro[b]

[a] *CEHINAV, ETSIN, Universidad Politécnica de Madrid (UPM), 28040 Madrid, Spain*

[b] *Instituto Nacional de Técnica Aeroespacial (INTA - CEHIPAR), 28048 Madrid, Spain*

[c] *CEHINAV, Departamento de Fisica Aplicada a la Ing. Aeronautica y Naval, ETSIN, UPM, 28040 Madrid, Spain*

[d] *CEHINAV, DACSON, ETSIN, UPM, Madrid, Spain, 28040 Madrid, Spain*

Abstract

Semi-submersible floating wind turbines are predicted to contribute significantly to the world energy supply in the coming decades. Scale effects are one of the most critical problems concerning the accuracy of model-scale experiments on these types of offshore structures. The current research aimed to assess the impact of the scale factor on the flow physics of semi-submersible platforms. Forced oscillation flow visualisation model-scale experiments on three geometrically similar one-leg columns of a semi-submersible platform equipped with a circular solid flat heave plate were performed. The experimental campaign was conducted in the Calm Water Towing Tank at INTA-CEHIPAR, Madrid, Spain. The forced oscillation tests were performed in the range of extreme and operational Keulegan-Carpenter numbers (KCs) for two different frequencies of the heave plate's oscillatory motion. A submersible two-dimensional (2D) three-component (3C) Stereoscopic Particle Image Velocimetry (Stereo-PIV) system was employed to measure the flow field velocity distribution. The Stereo-PIV images were obtained at four positions in the oscillation cycle. The investigation focused on detecting scale effects on the velocity and vorticity for the three models of different scales. Similarities in centre positions, shape, and contours between the three models were visualised for the measured velocity field. The computed vorticity field also revealed similarities in centre positions, shape, and contours among the three different scales. Following up previous works focusing on the hydrodynamic forces, the outcomes of this paper also confirm that the correct choice of the motion amplitude (KC) impacts the flow physics of the model tests more than the scale factor.

Keywords: Scale effects; Heave plate; Semi-submersible platform; Offshore wind turbine; SPIV; Vortex shedding, CFD validation.

Nomenclature

Acronyms

AR	aspect ratio
f/1	ratio of the system's focal length to the diameter of the entrance pupil
FoV	Field of View
Fr	Froude number
IA	interrogation area
KC	Keulegan–Carpenter number
LESs	large-eddy simulations
PIV	particle image velocimetry
Re	Reynolds number
SNR	signal-to-noise ratio
SPIV	stereoscopic particle image velocimetry
TBP	Time between pulses
UOD	Universal Outlier Detection

Greek Symbols

β	dimensionless frequency parameter
λ	scale factor
μ	water dynamic viscosity
ν	water kinematic viscosity
ω	angular frequency of the heave plate's oscillatory motion
ω_h	natural heave frequency
ω_X	x-component of the vorticity vector $\vec{\omega}$
$\overline{x_\omega^{\max}}$	averaged maximum vorticity location
$\overline{x_\omega^{\min}}$	averaged minimum vorticity location
ρ	water density
$\vec{\omega}$	vorticity vector
$x_\omega^{\max}$	maximum vorticity location
$x_\omega^{\min}$	minimum vorticity location

Roman Symbols

$\vec{V_R}$	velocity vector in the radial plane
$\vec{V_T}$	velocity vector in the tangential plane
$\vec{V}$	velocity vector
A	amplitude of the heave plate's oscillatory motion
$A_{33_{th}}$	theoretical added mass
D_c	column diameter
D_D	heave plate external disk diameter
f	frequency of the heave plate's oscillatory motion
g	gravitational acceleration
h	heave plate submergence
h/R_D	depth-radius ratio
h_b	disc distance to the bottom
L_c	column length
M	one-leg column mass
R_D	heave plate external disk radius
S_W	waterplane area
T	period of the heave plate's oscillatory motion
t	time
t_D	heave plate thickness
t_D/D_D	disc aspect ratio
V_D	maximum heave velocity of the plate's oscillatory motion
V_X	phase-averaged x-component of the velocity vector $\vec{V_T}$ in the tangential plane
V_Y	phase-averaged y-component of the velocity vector $\vec{V_R}$ in the radial plane
V_{MDR}	dimensionless velocity magnitude for the radial plane
V_{MDT}	dimensionless velocity magnitude for the tangential plane
V_{MR}	$V_M = \sqrt{V_Y^2 + V_{ZR}^2}$
V_{MT}	$V_M = \sqrt{V_X^2 + V_{ZT}^2}$
V_{ZR}	phase-averaged z-component of the velocity vector $\vec{V_R}$ in the radial plane
V_{ZT}	phase-averaged z-component of the velocity vector $\vec{V_T}$ in the tangential plane
(x, y, z)	Cartesian coordinate system

1. Introduction

The energy sector significantly contributes to atmospheric pollution and climate change. Fossil fuels are responsible for approximately 81% of global CO_2 emissions between 1959 and 2019 [1]. Depending on the future financial developments and growth of the energy sector, the CO2 emissions generated by the maritime industry are predicted to increase by 50% to 250% before 2050 [2]. Fulfilling the Kyoto Protocol's targets and the goals of the Paris Agreement require the accelerated deployment of renewable energies [3]. Wind power is a fossil-fuel-free energy source predicted to transform the global electricity sector in the coming decades. A large part of wind power generators is expected to be deployed in deep water areas [4], with estimations of almost a ten-fold increase in global capacity from 2019 to 2030 [5]. The importance of accurately estimating the seakeeping abilities of offshore wind farms is, therefore, undeniable.

Among the potential designs for floating wind technologies, semi-submersible wind turbine platforms have become increasingly popular in recent years [6]. The natural frequencies in pitch and roll of these offshore structures are generally lower than 0.04 Hz, below the typical frequency spectrum of ocean waves. However, the natural heave frequency of semi-submersible platforms usually falls within the first-order ocean wave range. Damping-augmenting devices, such as thin plates installed at the structure's base, are commonly employed to introduce additional hydrodynamic damping (by intensifying the vortex shedding process) and to decrease the natural frequency of the platform (by increasing the heave added mass) [7]. The vertical response of the structure is influenced by the shape and location of the heave plate [8].

Thiagarajan [9] carried out Particle Image Velocimetry (PIV) model-scale experiments for two oscillating circular solid disks of different thicknesses: disk A and B. The former had a uniform thickness (6.35 mm), whereas the latter had infinitesimal thickness at the edge (2.54 mm at the centre, tapering off to 0.1 mm at the edge). The Keulegan–Carpenter number ranged from 0.131 to 0.524, whereas the Reynolds number (Re) varied from 655 to 6550. The water tank used for the experiments had dimensions equal to 0.61 x 0.61 x 0.76 m. The disk of uniform thickness exhibited symmetric flow about the mean position of the oscillation for Reynolds numbers lower than 1965. The vorticity shed from the edges was found to roll up into vortex rings, which remained close to the disk until flow reversal caused a prompt cancellation of vorticity. The disk of infinitesimal thickness at the edge revealed an asymmetric vortex shedding pattern for Reynolds numbers lower than 2620. The vortices generated during successive half-cycles formed vortex pairs that convected away from the edges. Based on these observations, it was concluded that the hydrodynamic damping of disk B was larger than disk A (for a given KC and dimensionless frequency parameter β) because of the higher energy dissipation caused by the different vortex formation. He et al. [10] conducted flow visualization model-scale experiments on three oscillating circular solid disks with thickness-to-diameter ratios between 1/87.5 and 1/25, KC ranging from 0.01 to 1.1, and dimensionless frequency parameter β varying from $6 \cdot 10^3$ to $4.8 \cdot 10^4$. The towing tank had dimensions equal to 1.73 x 0.97 x 1.22 m. The investigation of the flow physics revealed that the interaction of vortices generated from the disk corners plays a crucial role in damping effectiveness. An increase in thickness resulted in a decreased interaction between the newly generated vortices and those previously created. This phenomenon caused a reduction in hydrodynamic damping as the thickness-to-diameter ratio of the disk increased.

In addition to model-scale experiments on oscillating disks, examining the vortex formation of towed plates provides essential knowledge on how the hydrodynamic forces

are affected by the fluid flow behaviour. Fernando and Rival [11] studied the role of edge discontinuities and non-uniform curvatures on the vortex formation by towed low-aspect-ratio solid elliptical and rectangular flat plates. The Reynolds number was approximately 10^3, whereas the aspect ratio (AR) varied from 1.0 to 4.0. The wake dynamics of the plates was assessed by PIV. The experiments were carried out in a 4 m-long towing tank with a 0.45 x 0.40 m cross-section. This work indicated that the aspect ratio is the main parameter to describe the vortex-ring evolution for the selected case studies. Edge discontinuities and non-uniform curvatures played only a secondary role in the vortex formation. In the context of investigating the biomechanics of animal propulsion, Fernando and Rival [12] also investigated the vortex-ring evolution of towed low-aspect-ratio solid elliptical and rectangular flat plates as a function of the Reynolds number. A PIV system was utilised to measure the vortex growth in the wake of the plates. The Reynolds number ranged from $5 \cdot 10^4$ to $3.5 \cdot 10^5$, while the aspect ratio varied from 1.0 to 2.0. The experiments were carried out in a towing tank of 1 m^2 cross-sectional area and a total length of 15 m. For the plates with an aspect ratio close to 2.0, vortex dynamics appeared to be independent of the Reynolds number and peaks in the force signals were noticed (indicating better suitability for braking situations and manoeuvring). For the plate with an aspect ratio of 1.0, the Reynolds number influenced the vortex-ring evolution, and the plate forces were comparatively low. The results presented in this work provided a plausible explanation for the extensive appearance of propulsors with AR greater than one in biological entities. Satheesh and Huera-Huarte [13] examined the wake region's evolution of towed solid low-aspect-ratio rectangular plates as a function of the Reynolds number and submergence depth. The flow visualisation analysis was carried out by utilising a PIV system. The aspect ratio ranged from 0.25 to 4.0. The Reynolds number varied from $3 \cdot 10^4$ to $6 \cdot 10^4$. The towing tank had dimensions equal to 0.6 x 0.6 x 2 m. The results showed an increase in drag caused by the reduction in submergence depth. This increment in drag was related to the formation of asymmetric recirculating flow at the base region of the plate.

The previously mentioned flow visualisation experiments mainly focused on the hydrodynamic characteristics of oscillating plates and plates towed at a constant speed related to their geometric shapes. However, scale effects are one of the most critical concerns regarding the accuracy of hydrodynamic model tests. This is mainly because the Reynolds number of the model is usually two orders of magnitude lower than the one of the prototype. Two rare examples of this type of investigation are the works conducted by Tian et al. [14] and Anglada-Revenga et al. [15]. Tian et al. [14] studied the effect of the Reynolds number on the vortical structures of a solid oscillating flat circular disk by performing large-eddy simulations (LESs). The KC ranged from 0.2 to 1.0. The dimensionless frequency parameter β varied from $8 \cdot 10^2$ to $8 \cdot 10^6$. The flow was approximately axisymmetric for the lowest considered value of β, and the vortical rings were caused by laminar vortex shedding. On the other hand, for β larger than $8 \cdot 10^3$, the resulting vortical structures were non-axisymmetric and turbulent. Nevertheless, even though the flow regime was different at high and low Reynolds numbers, the hydrodynamic force coefficients acting on the disk were more dependent on the motion amplitude (KC) than on the scale of the model. Based on this outcome, it was concluded that scale effects could be considered negligible for heave plates, and the hydrodynamic forces can be computed by simply following the geometric similarity law. Following up on the work conducted by Bezunartea-Barrio et al. [16] on the impact of scale effects on the hydrodynamic forces of semi-submersible platforms, Anglada-Revenga et al. [15] studied the influence of the scale factor on the flow physics

of oscillating heave plates by performing PIV model-scale experiments. The investigation consisted of comparing the velocity and vorticity determined for three models of different scales. A Stereo Particle Image Velocimetry (SPIV) was utilised for the tests. The KC ranged from 0.157 to 0.628, and the Reynolds number of the three models varied from $1.1 \cdot 10^4$ to $5 \cdot 10^5$. The flow analysis showed similarity in the velocity field for the only case reported. Consequently, a conclusion was not drawn on the importance of scale effects on the vortex dynamics.

The present study extends the work conducted by Anglada-Revenga et al. [15] and Bezunartea-Barrio et al. [16] regarding the impact of scale effects on oscillating circular solid plates. Flow visualisation model-scale experiments were carried out on three geometrically similar one-leg columns of a semi-submersible platform equipped with a circular solid flat heave plate. A SPIV system was utilised to perform velocity field measurements of the flow. At the post-processing stage, particular attention was given to assessing the impact of scale effects on the velocity and vorticity variation. The post-processing data supporting the reported figures can be found as supplementing material in Section 8.

2. Case Study

Three geometrically similar one-leg columns of a semi-submersible platform equipped with a heave plate were selected as the model test cases (see Figure 1). These models were also utilised by Anglada-Revenga et al. [15] and Bezunartea-Barrio et al. [16]. The prototype was constructed in conjunction with the HiPRWind EU research project [17]. The structure of the semi-submersible floater consisted of three vertical columns connected by braces. The heave plates of the prototype were equipped with structural reinforcements. However, the selected models lacked any additional structure on the heave plates. This is because the current study solely aims at assessing the importance of scale effects for flat heave plates. The thickness diameter ratios of the three models were not perfectly geometrically similar. The largest model had a thickness diameter ratio of 0.005, whereas the two smallest models had a thickness diameter ratio of 0.003. The heave plate thicknesses are presumably sufficiently small to cause only minor variations in flow kinematics. The platform's main dimensions are provided in Table 1. Figure 2 shows the main geometrical parameters describing the models. Further details regarding the semi-submersible platform can be found in Simos et al. [18] and Lopez-Pavon et al. [19].

Fig. 1. Sketch of the semi-submersible wind turbine platform.

Table 1
Main dimensions of the platform (prototype and scaled models).

Symbol	Unit	λ_0=1	λ_1=20	λ_2=27.6	λ_3=45.45
M	[kg]	$663{\cdot}10^3$	82.83	31.50	7.10
h	[m]	15.5	0.775	0.562	0.341
D_c	[m]	7.0	0.350	0.254	0.154
L_c	[m]	23.8	1.192	0.864	0.525
D_D	[m]	20.0	1.000	0.725	0.440
R_D	[m]	10.0	0.500	0.362	0.220
t_D	[mm]		5.000	3.600	2.200
h/R_D	[-]	1.550	1.550	1.550	1.550
t_D/D_D	[-]		0.005	0.003	0.003
D_D/D_c	[m]	2.857	2.857	2.857	2.857
h_b/R_D	[-]		11.45	16.39	27.39

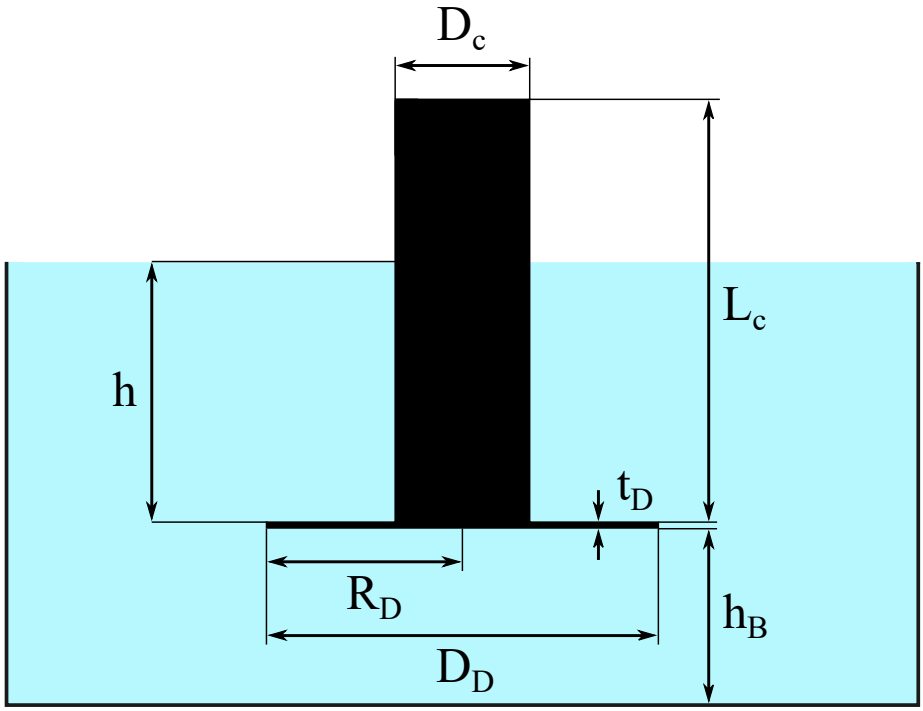

Fig. 2. Main geometrical parameters of the models.

3. Physical problem

The fluid properties were estimated for fresh water at standard conditions of 12°C and 1 atm: $\rho = 998.2072$ kg/m^3 and $\mu = 0.001002$ Pa·s. The Buckingham Pi theorem was

applied to derive the dimensionless parameters representing the physics of the problem tackled in the current study (model-scale experiments on oscillating disks for models of different scales). For shortness, only the results obtained with the Buckingham Pi theorem are reported. The detailed procedure can be found in the literature (e.g., Frémond et al. [20]).

3.1. Keulegan–Carpenter number

The Keulegan–Carpenter number is a dimensionless quantity representing the relative importance of the drag force over the inertia force for oscillating objects in a fluid at rest. The Keulegan–Carpenter number was defined as:

$$\mathrm{KC} = 2\pi \frac{A}{D_D}, \tag{1}$$

where A is the amplitude of the heave plate's oscillatory motion and D_D is the heave plate external disk diameter.

3.2. Reynolds number

The Reynolds number is a dimensionless quantity measuring the ratio of inertial forces to viscous forces. The Reynolds number was defined by considering the maximum heave velocity of the plate's oscillatory motion V_D:

$$\mathrm{Re} = \frac{\rho A\,\omega\,D_D}{\mu} = \frac{\rho\,V_D\,D_D}{\mu}, \tag{2}$$

where ω is the angular frequency of the heave plate's oscillatory motion. The Reynolds number ranged from $9.3 \cdot 10^3$ to $3.9 \cdot 10^5$.

3.3. Froude number

The Froude number is a dimensionless quantity representing the ratio of inertial forces to the external forces (usually gravity). The Froude number was defined by considering the maximum heave velocity of the plate's oscillatory motion V_D and the plate's depth h:

$$\mathrm{Fr} = \frac{A\,\omega}{\sqrt{g\,h}} = \frac{V_D}{\sqrt{g\,h}}, \tag{3}$$

where g is the gravitational acceleration. The depth-radius ratio of the heave plate was equal to 1.55. This value can be considered large for submerged heave plates. As a result, the viscous damping was expected to be much larger than the propagation of energy away from the structure by motion-induced waves (wave radiation damping). Based on this consideration, the Froude number was not further considered in the present study.

3.4. Dimensionless frequency parameter

The dimensionless frequency parameter β is commonly employed when considering cylinders oscillating sinusoidally in a fluid at rest. It was defined as the ratio of the Reynolds number to the Keulegan–Carpenter number:

$$\beta = \frac{\mathrm{Re}}{\mathrm{KC}} = \frac{\rho\,f\,D_D^2}{\mu}, \tag{4}$$

where f is the frequency of the heave plate's oscillatory motion. The dimensionless frequency parameter β ranged from $5.9 \cdot 10^4$ to $6.2 \cdot 10^5$.

3.5. Undamped natural heave frequency

The undamped natural heave frequency ω_h is the frequency at which the one-leg column tends to oscillate vertically in the absence of any driving or damping force. The theoretical added mass $A_{33_{th}}$, determined as indicated by Sarpkaya et al. [21], was utilized to calculate ω_h:

$$\omega_h = \left(\frac{\rho \, g \, S_W}{M + A_{33_{th}}} \right)^{0.5}, \tag{5}$$

where S_W is the waterplane area and M is the one-leg column mass. The theoretical added mass was further corrected by considering the cylindrical column volume, as suggested by Tao et al. [22]. The corresponding full-scale natural heave period was estimated to be 17.9 s.

4. Model-scale tests

4.1. Test set-up

The experimental campaign was conducted in the Calm Water Towing Tank at INTA-CEHIPAR, Madrid, Spain. Its main dimensions are 320 m in length, 12.5 m in width, and 6.5 m in depth. The experiments were conducted in the middle of the towing tank (longitudinally and transversally) to minimise wave reflection issues. The ratio between the distance to the bottom h_b and the disc radius R_D was sufficient large not to create bottom effects (minimum value larger than 10).

The forced heave motions of the models were generated by two electric actuators (Servomotor Yaskawa SGMG-13V-1.3KW). The actuators were directly attached to the towing carriage. The models were connected to the actuators through an aluminium bar (Bosch profile). A high-resolution digital encoder was utilized to record the vertical motions. The maximum vertical speed of the oscillatory motions was 0.45 m/s. A SPIV system attached to the towing carriage was utilized for the flow physics investigation. All the tests started from the same initial position with a zero vertical velocity. The waiting time between consecutive runs was set to obtain comparable conditions for each run and produce consistent results. Figure 3 shows a photo of the experimental setup.

To the best of the author's knowledge, the current study is a unique case where PIV measurements on oscillating heave plates are performed in a large scale basin. The experimental setup and procedure were based on the author's knowledge of other types of PIV experiments, e.g. the European Union (EU) project "Achieve QUieter Oceans by shipping noise footprint reduction" (AQUO) [23].

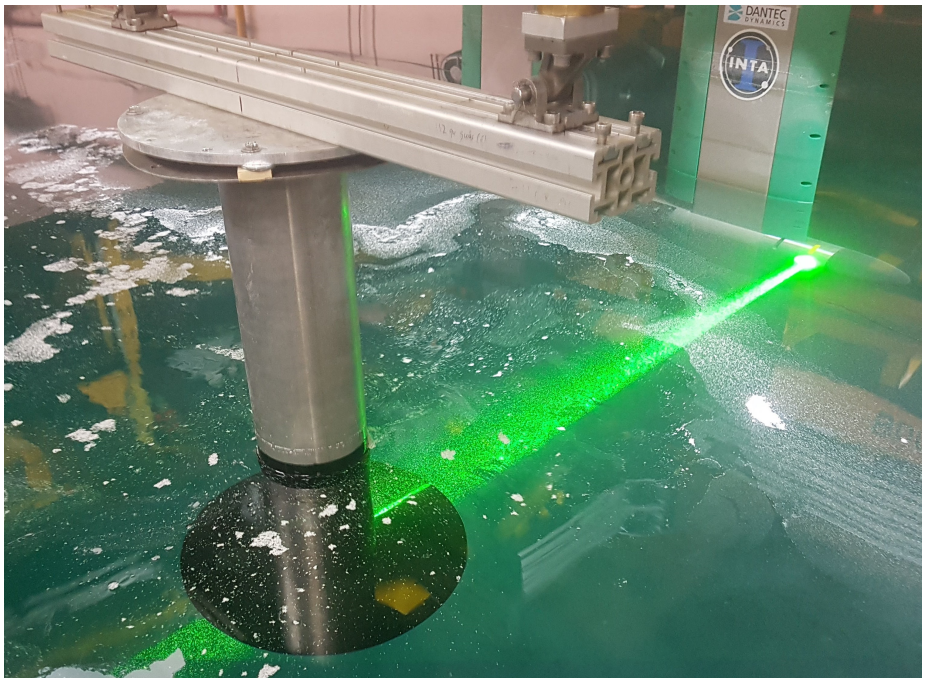

Fig. 3. Overview of the experimental setup.

4.2. Model-test program

Table 2 displays the 144 test conditions carried out in the experiments. Two dimensionless frequencies, ω_{1h} and ω_{2h}, (nondimensionalized with the undamped natural heave frequency ω_h) were considered. Three Keulegan–Carpenter numbers, KC_1, KC_2, and KC_3 (corresponding to extreme and operational conditions), were selected. Two measurement planes, tangential and radial to the flat heave plate, were captured (see Figure 4). SPIV images were captured at consecutive cycles, and the flow field proprieties were phase averaged (see Section 4.3 for more details). Four positions in the oscillation cycle were studied, i.e. Figure 5.

- A: heave plate positioned at the top of its amplitude, $t/T = 0.75$,
- B: heave plate located at zero position (moving down), $t/T = 0.00$,
- C: heave plate placed at the bottom of its amplitude, $t/T = 0.25$,
- D: heave plate located at zero position (moving up), $t/T = 0.50$,

where t is the time counting from the start of each cycle and T is the motion period (the plate always had an initial downwards motion).

Table 2
Test conditions carried out in the experiments for the three models: two measurement planes, two frequencies, three KCs, and four positions in the oscillation cycle.

Plane	Frequency	Amplitude	Scale	Position
Radial	ω_{1h}=1.000	KC_1=0.628	λ_1, λ_2, λ_3	A, B, C, D
		KC_2=0.314	λ_1, λ_2, λ_3	A, B, C, D
		KC_3=0.157	λ_1, λ_2, λ_3	A, B, C, D
	ω_{2h}=3.079	KC_1=0.628	λ_1, λ_2, λ_3	A, B, C, D
		KC_2=0.314	λ_1, λ_2, λ_3	A, B, C, D
		KC_3=0.157	λ_1, λ_2, λ_3	A, B, C, D
Tangential	ω_{1h}=1.000	KC_1=0.628	λ_1, λ_2, λ_3	A, B, C, D
		KC_2=0.314	λ_1, λ_2, λ_3	A, B, C, D
		KC_3=0.157	λ_1, λ_2, λ_3	A, B, C, D
	ω_{2h}=3.079	KC_1=0.628	λ_1, λ_2, λ_3	A, B, C, D
		KC_2=0.314	λ_1, λ_2, λ_3	A, B, C, D
		KC_3=0.157	λ_1, λ_2, λ_3	A, B, C, D

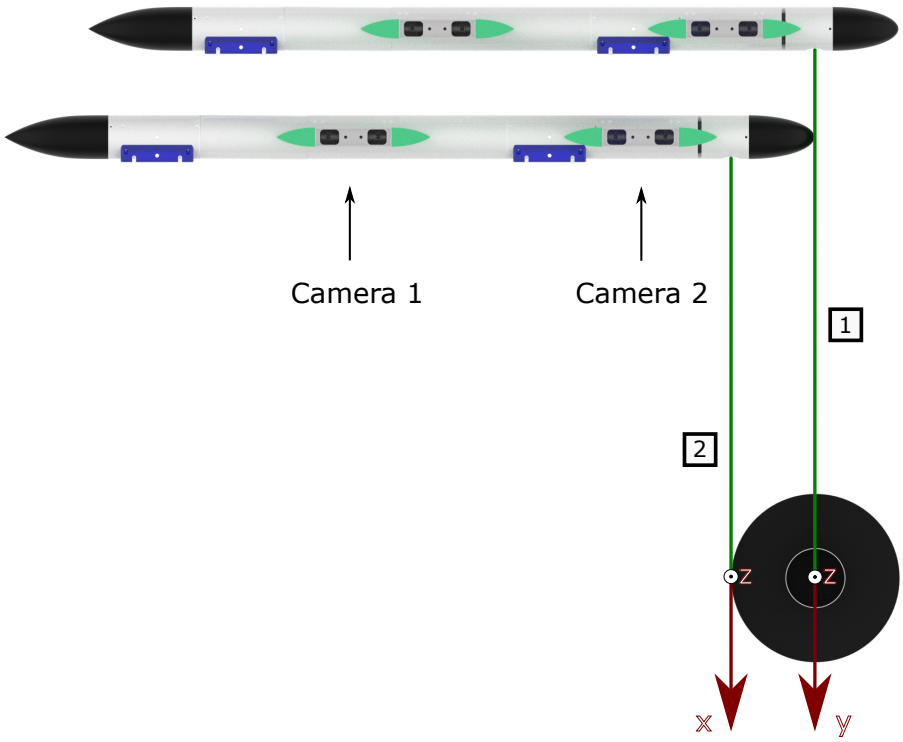

Fig. 4. 2D schematic of the SPIV system. 1: Radial plane. 2: Tangential plane.

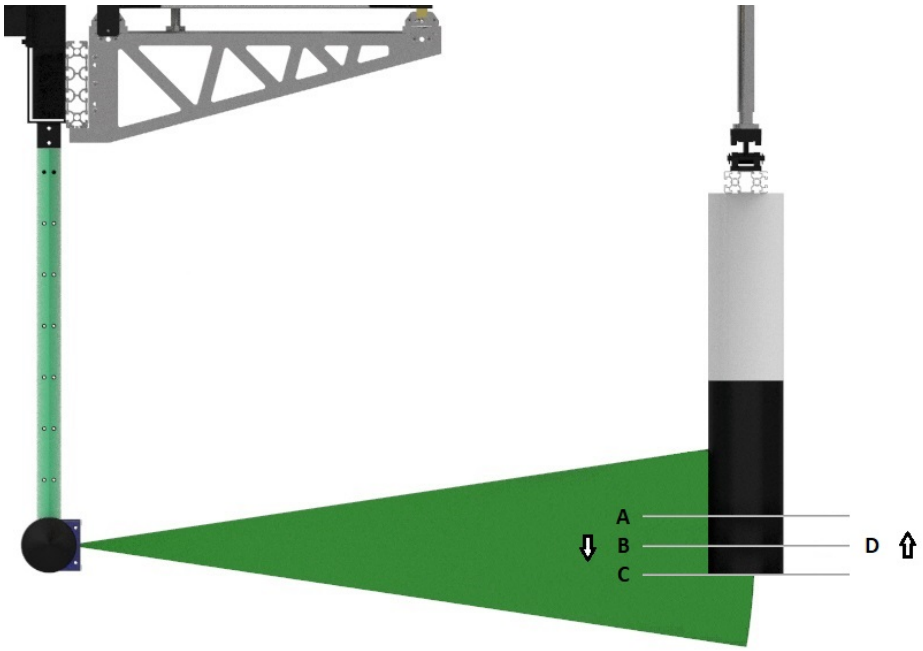

Fig. 5. Measuring points: B ($t/T = 0.00$, zero-down), C ($t/T = 0.25$, bottom), D ($t/T = 0.50$, zero-up), and A ($t/T = 0.75$, top).

4.3. SPIV

Particle Image Velocimetry is a non-intrusive laser optical measuring technique capable of capturing the instantaneous velocity distribution (two or three components) in a planar section of a fluid. The flow field is captured by quantifying the movement of tracer particles transported by the flow. These seeding particles are illuminated twice by a laser sheet at a small-time delay (time between pulses, TBP), and a digital imaging device (usually one or two digital cameras) records the light scattered by the particles on the two subsequent frames. Further details on PIV systems can be found in Raffel et al. [24].

In this research project, a submersible 2D-3C Stereo-PIV system manufactured by Dantec Dynamics was utilized (see Figure 4). This system utilised two digital cameras to extract the three components of the velocity vector in a two-dimensional measurement plane. The digital cameras were located at one side of the laser (asymmetrical configuration). A double-pulse laser (Nd:YAG system) with a maximum acquisition frequency of 15 Hz was used. Two standard FlowSense 4M MKII CCD cameras (2024 x 2024 pixels - 8 bits per pixel) were placed in a watertight compartment inside a submerged probe. The digital cameras were equipped with 50 mm f/1:1.8 and 85 mm f/1:1.8 lenses because of the asymmetrical configuration of the SPIV system. The Scheimpflug principle was satisfied to overcome focusing problems in the angular displacement. The submerged probe was connected to the towing tank carriage with a traverse system, which allowed a high accuracy positioning of the laser sheet. White spheroidal polyamide seeding particles with an average diameter of 60 μm and a density approximately equal to the water density were utilised for the measurements. A

simple mechanical in-house swirl mixing generator was developed to create a good homogenous seeding-water mixture close to the measurement area. Specifically, the seeding-water mixture was created, outside the towing tank, by applying a high shear stress force. Then, the mixture was spread close to the measurement area before starting the experiment. This procedure was repeated every one or two tests depending on the frequency of the heave plate's oscillatory motion. An encoder and a trigger were utilized to synchronize the acquisition of the images at the required amplitude points with a delay lower than 4.0 μs.

The time between pulses, the number of images to be averaged, and the sampling frequency were precisely established. The TBP values were based on the vertical speed of the heave plate. A parametric study was conducted to determine the number of images necessary to measure the vortex shedding pattern adequately. The number of images was varied systematically, and the measured velocity components and their standard deviations were compared. This study showed that 50 cycles were sufficient to define the flow field. In each cycle, one pair of images was recorded. This setup implied that the sampling frequency was set equal to the cylinder's oscillatory motion frequency.

5. Analysis of the results

5.1. Coordinate system

Two separate 2D Cartesian coordinate systems (see Figure 4) were utilized to identify the radial and tangential planes:

- *Radial plane* - *Coordinate system YZ*: z-axis positive upwards, y-axis negative towards the location of the cameras, and origin located at the resting position of the disk centre.
- *Tangential plane* - *Coordinate system XZ*: z-axis positive upwards, x-axis negative towards the location of the cameras, and origin located at the resting position of the disk edge.

If the origin of the coordinate system XZ is moved on top of the origin of the coordinate system YZ and the coordinate system XZ is ninety degrees rotated around the z-axis, a cylindric coordinate system will be obtained. Figure 6 shows the resulting position of the measured radial and tangential plane under this case.

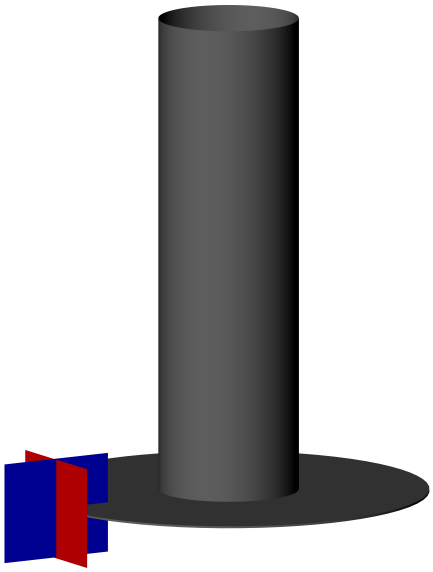

Fig. 6. Radial plane (blue) and ninety degrees rotated tangential plane (red).

5.2. PIV data

The data acquisition, pre-processing, and post-processing were carried out by the commercial software DynamicStudio 6.4 [25]. A background subtraction method based on the mean of all the images captured in each test was applied. An "Adaptive PIV" algorithm was utilized to estimate the particle displacement. This algorithm was based on a cross-correlation, adaptive, and iterative procedure. The displacement was calculated on an adapting interrogation area (IA). The minimum amount of detected particles was set to be at least 10, the peak ratio was equal to 1.15, and the IA overlapping was selected to be 50%. Several validation schemes were employed, such as peak height ratio, peak height, and SNR & Universal Outlier Detection (UOD). The false vectors were substituted based on the average value of the surrounding vectors.

5.3. Velocity field definition

The in-plane velocity field was defined as follows:

$$V_{MDR} = \frac{V_{MR}}{V_D}, \qquad V_{MR} = \sqrt{V_Y^2 + V_{ZR}^2}\,, \qquad \vec{V_R} = (V_Y, V_{ZR}), \tag{6}$$

$$V_{MDT} = \frac{V_{MT}}{V_D}, \qquad V_{MT} = \sqrt{V_X^2 + V_{ZT}^2}\,, \qquad \vec{V_T} = (V_X, V_{ZT}), \tag{7}$$

where $\vec{V_R}$ is the velocity vector in the radial in-plane, $\vec{V_T}$ is velocity vector in the tangential in-plane, V_X is the x-component of the velocity vector $\vec{V_T}$, V_Y is the y-

component of the velocity vector $\vec{V_R}$, V_{ZT} is the z-component of the velocity vector $\vec{V_R}$, V_{ZR} is the z-component of the velocity vector $\vec{V_R}$, V_{MRD} is the dimensionless velocity magnitude in the radial in-plane, and V_{MRT} is the dimensionless velocity magnitude in the tangential in-plane.

5.4. Flow analysis

The Field of View (FoV) of the SPIV cameras was model-scale independent and approximately equal to 250 mm × 300 mm. As a result, the bigger the model, the higher the information density of the recorded images. Based on this, the velocity and vorticity had to be interpolated to conduct the comparison among the scales. For this purpose, a Python script was developed. The velocity fields obtained by Dynamic-Studio 6.4 were spatially interpolated onto common grids. Several grid densities were tested, and the velocity and vorticity fields were compared. The maximum velocity was consistent among the different grids, with a maximum relative variation of ±1.6%. However, the vorticity field was more affected by the grid resolution. Specifically, the relative increase in maximum and decrease in minimum vorticity among the three scales diverged with the increase of the grid density, but converged for low-resolution grids. Therefore, the velocity field analysis was conducted on grids with a density similar to the largest scale velocity field. Instead, the vorticity was computed by utilising velocities interpolated on grids with a density close to the smallest scale velocity field. The SciPy Python library was employed to interpolate the velocity data. Two grid interpolation methods, linear and cubic, were also compared. The comparison revealed negligible differences between the two interpolation techniques (indicating that the overshoot problem at intermediate points caused by the piecewise cubic interpolation was avoided). Consequently, the cubic interpolation method was chosen for the current analysis because of its smoothness. The Matplotlib Python library was used for the data visualisation.

5.5. Instantaneous velocity uncertainties

The quality of the 50 images recorded in each test case was determined by computing the precision error $\bar{e}_s$ defined in Equation 8:

$$\bar{e}_s = \frac{t_s \cdot S_x}{\sqrt{N} \cdot M}, \tag{8}$$

where t_s is t-distribution, S_x is the standard deviation of the velocity, N is the number of images, and M is the mean of the maximum velocities in the N recorded FoVs. The two-tailed Student's t-distribution with N-1 degrees of freedom was calculated with a cumulative probability of 0.95.

Figure 7 shows two representative examples of the instantaneous velocity in comparison with the phase-averaged velocity for the radial in-plane. The general trend indicated a small change of the maximum velocity magnitude, $\bar{e}_s$ approximately equal to 3% to 4% depending on the case, and an acceptable deviation of the velocity field's shape and contours.

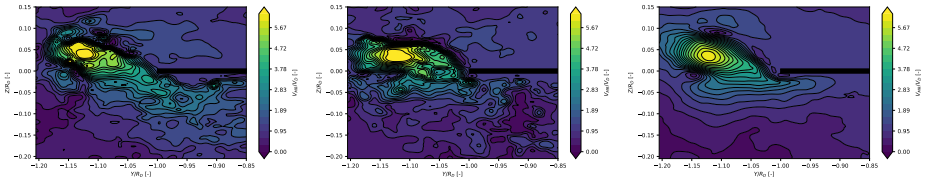

Fig. 7. V_{MR}/V_D - YZ radial plane with heave plate (black rectangle) - Case: ω_{1h}, KC_3, λ_1, and position $t/T = 0.00$ (zero-down) for two instantaneous velocity field (left and middle) and the phase-averaged velocity field (right).

The precision error $\bar{e}_s$ was also calculated by considering the variation of the velocity at the same spatial position among the 50 pairs of images. Figure 8 presents a representative example along with the phase-averaged velocity field for the radial in-plane. The precision error is approximately equal to 4-9% in the area of maximum velocity magnitude depending on the case.

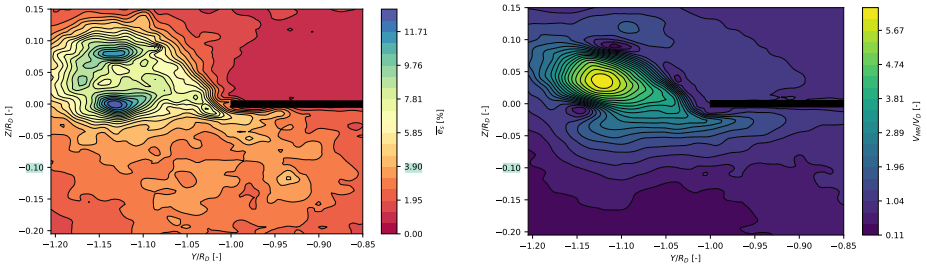

Fig. 8. Precision error $\bar{e}_s$ (left) and phase-averaged velocity field V_{MR}/V_D (right) - YZ radial plane with heave plate (black rectangle) - Case: ω_{1h}, KC_3, λ_1, and position $t/T = 0.00$ (zero-down).

6. Results

All the main quantities were nondimensionalized to facilitate the comparison between different scale ratios:

- Velocities were divided by the maximum heave velocity of the plate's oscillatory motion V_D.
- Vorticity was divided by the angular frequency of the heave plate's oscillatory motion ω (the vorticity is equal to twice the local fluid angular velocity).
- Lengths were divided by the heave plate external disk radius R_D.

6.1. Radial in-plane

As beforementioned, the SPIV measurements provided all three velocity components. However, the out-of-plane velocity components were one order of magnitude lower than the in-plane velocity components. Furthermore, a larger kinetic energy flow was expected in the radial plane than in the tangential plane because of the heave plate's axisymmetric geometry. This hypothesis was confirmed by comparing the dimensionless velocity magnitudes in the radial in-plane V_{MRD} and the tangential in-plane V_{MRT}. Two-dimensional filled contour plots were utilized for the analysis. The tangential plane was rotated ninety degrees (z-axis rotated) and placed on the radial plane to have a straightforward comparison (see Figure 6). For clarity, the heave damping plate was added to the plot as a black disk. Figure 9 shows a representative example (ω_{1h}, KC_3, λ_2, and position $t/T = 0.25$, zero-down) of the performed examination. First, it is possible to appreciate the continuity of the velocity field at the intersection of the planes. Second, the radial plane (left) exhibits much larger velocities and gradients than the tangential plane (right). Consequently, including the tangential plane in the analysis of the scale effects would be nonessential for the current study. Based on these results, the scale effect analysis focuses only on the radial in-plane.

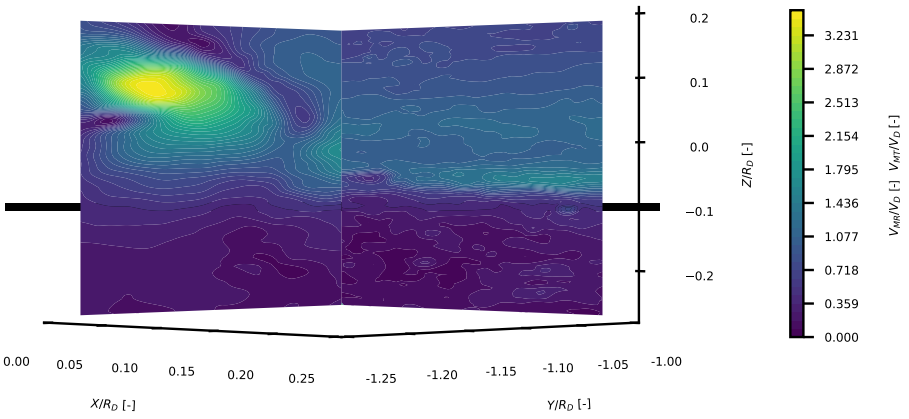

Fig. 9. V_{MR}/V_D and V_{MT}/V_D - YZ radial plane (left) and XZ tangential plane (right) with heave plate (black disk) - Case: ω_{1h}, KC_3, λ_2, and position $t/T = 0.25$ (bottom).

6.1.1. Velocity magnitude

The scale effect analysis on the flow was carried out by analysing and visually examining the dimensionless velocity magnitude V_{MDR} (see Equation 6). Two-dimensional contour line plots and two-dimensional filled contour plots (with the heave damping plate included as a black rectangle) were utilised for the visual graph analysis.

The first investigation was performed by varying only the scale ratio and keeping all the other parameters constant. Figure 10 displays a representative example (ω_{1h}, KC_3, and position $t/T = 0.25$, bottom) of the performed study for the three scale ratios (λ_1, λ_2, and λ_3). Figure 11 shows the dimensionless velocity magnitude at the lowest and highest scale ratios (λ_1 and λ_3) for another representative example (ω_{1h}, KC_3, and position $t/T = 0.00$, zero-down).

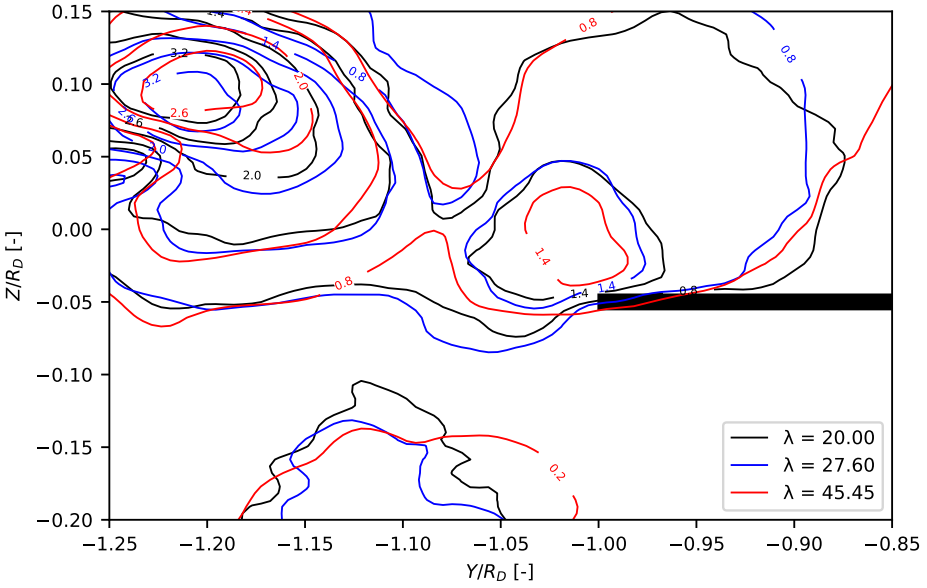

Fig. 10. V_{MR}/V_D contours - YZ radial plane with heave plate (black rectangle) - Case: ω_{1h}, KC_3, λ_1 (black), λ_2 (blue), λ_3 (red), and position $t/T = 0.25$ (bottom).

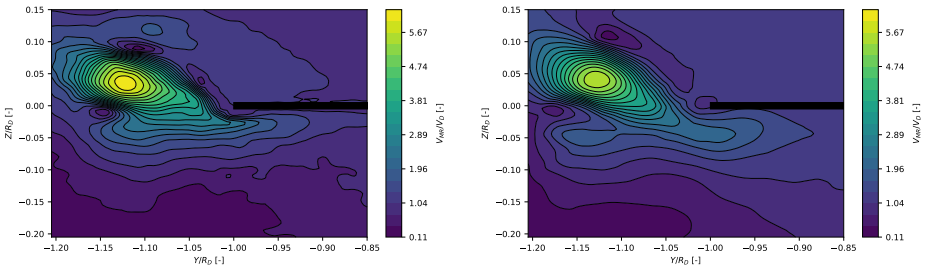

Fig. 11. V_{MR}/V_D - YZ radial plane with heave plate (black rectangle) - Case: ω_{1h}, KC_3, λ_1 (left), λ_3 (right), and position $t/T = 0.00$ (zero-down).

The analysis revealed a small increase in the dimensionless velocity magnitude for increasing scale ratios (e.g., approximately 8% to 14% between λ_1 and λ_3 depending on the case). The location of the maximum velocity magnitude appeared to be negligibly influenced by the dimension of the model. The velocity field's shape and contours also seemed to be consistent among the three scales.

The second investigation was carried out by varying only the angular frequency of the heave plate's oscillatory motion and keeping all the other parameters constant (scale ratio included). Figure 12 displays the dimensionless velocity magnitude over the two angular frequencies (ω_{1h} and ω_{2h}) for a representative example (λ_1, KC_3, and position $t/T = 0.25$, bottom).

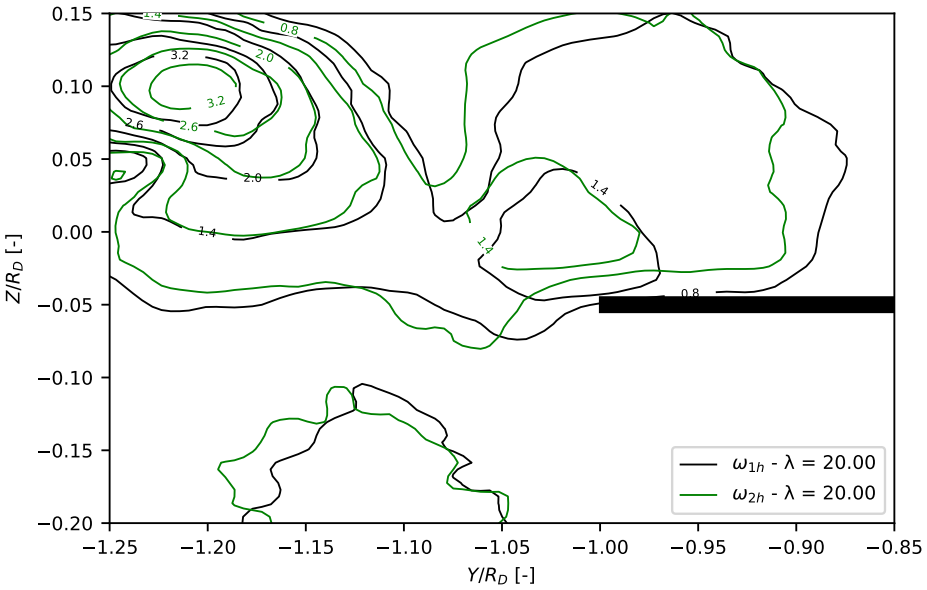

Fig. 12. V_{MR}/V_D contours - YZ radial plane with heave plate (black rectangle) - Case: ω_{1h} (black), ω_{2h} (green), KC_3, λ_1, and position $t/T = 0.25$ (bottom).

This investigation reported a small decrease in the dimensionless velocity magnitude for increasing angular frequencies (e.g., approximately 6% to 16% for λ_1 depending on the case). Additionally, the position of the maximum velocity magnitude was minimally affected by the angular frequency of the heave plate's oscillatory motion. The velocity field's contours and shape were also consistent between the two frequencies.

6.1.2. Velocity direction

Streamline plots (with the heave damping plate included as a black rectangle) were employed to examine scale effects on the velocity direction. Figure 13 and Figure 14 show an example of the performed streamline comparison for the two angular frequencies of the heave plate's oscillatory motion (ω_{1h} and ω_{2h}) for a representative case (KC_2 and position $t/T = 0.75$, top).

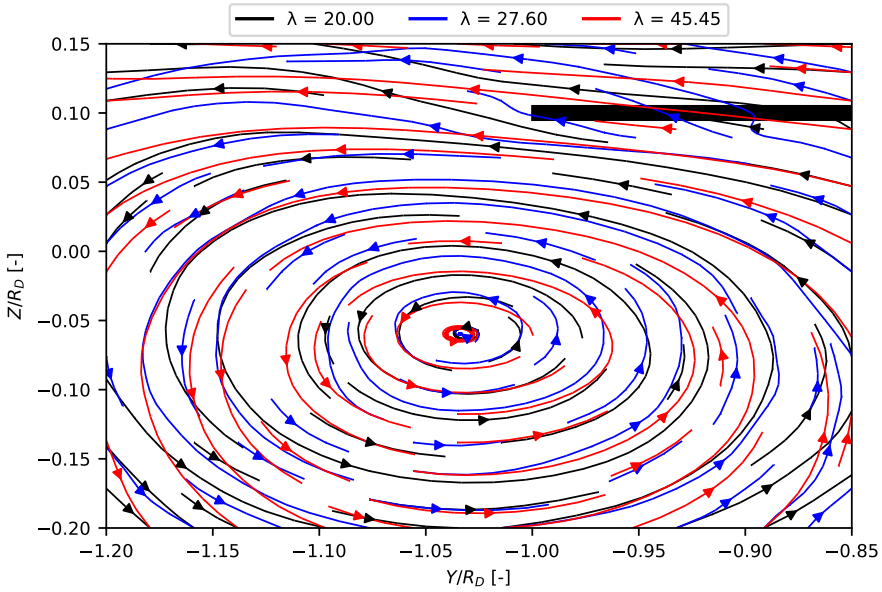

Fig. 13. Streamlines - YZ radial plane with heave plate (black rectangle) - Case: ω_{1h}, KC_2, λ_1 (black), λ_2 (blue), λ_3 (red), and position $t/T = 0.75$ (top).

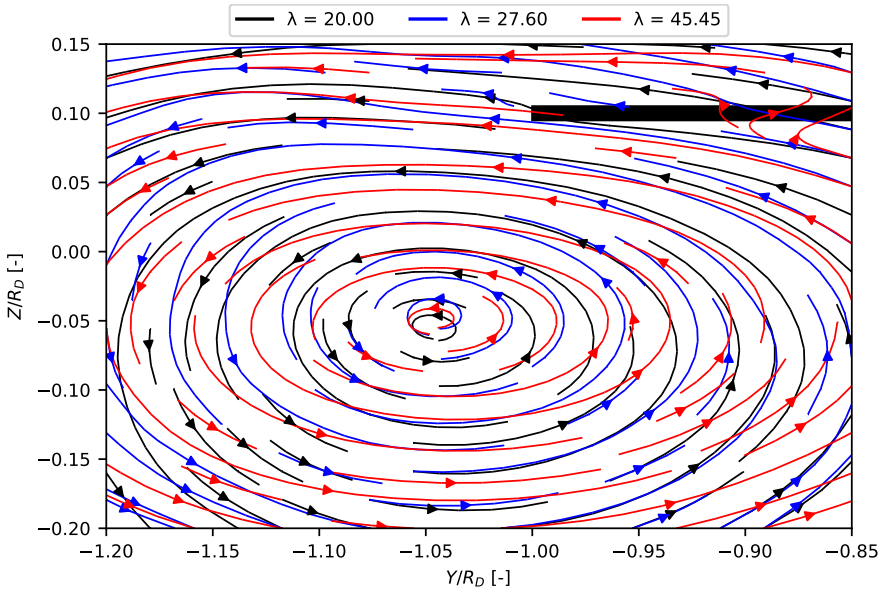

Fig. 14. Streamlines - YZ radial plane with heave plate (black rectangle) - Case: ω_{2h}, KC_2, λ_1 (black), λ_2 (blue), λ_3 (red), and position $t/T = 0.75$ (top).

Minimum differences were observed among the closed curves tangent to the averaged velocity field for three scale ratios (especially in the primary vortex structures). This result indicated that the dimensions of the model had a small impact on the velocity direction.

6.1.3. Vorticity

Flow separation at the edge of the heave plate leads to generating a substantial amount of vorticity in every oscillation cycle. Vorticity generation is connected to the dissipative properties of the flow. Indeed, Garrido-Mendoza et al. [26] showed that the vorticity field could be used to estimate the linearised damping coefficient by tracking the time evolution of the enstrophy (volume integral of the square of the vorticity). This volume integral cannot be carried out accurately with the experimental data due to the limited size of the PIV windows. However, this does not reduce the interest in assessing the influence of the scale factor, KC, and frequency on the vorticity field. The curl of the velocity field computed in the in-plane velocity component represented the largest part of the three-dimensional vorticity in the radial plane. Consequently, the vorticity vector $\vec{\omega}$ was assumed to be parallel to the x-axis and, therefore, it could be expressed as the scalar field ω_X multiplied by the constant unit vector $\vec{x}$:

$$\vec{\omega} = \nabla \times \vec{V} = \left(\frac{\partial V_Z}{\partial Y} - \frac{\partial V_Y}{\partial Z} \right) \vec{x} \,, \qquad \omega_X = \frac{\partial V_Z}{\partial Y} - \frac{\partial V_Y}{\partial Z} . \tag{9}$$

Two-dimensional filled contour plots (with the heave damping plate included as a black rectangle) were utilised for the visual graph analysis. As performed for the velocity magnitude, the first analysis was carried out by varying only the scale ratio and keeping all the other parameters constant. Figure 15 and Figure 16 show two representative examples (KC_3 and position $t/T = 0.00$, zero-down) of the vorticity comparison carried out over the three scale ratios (λ_1, λ_2, and λ_3) for the two angular frequencies of the heave plate's oscillatory motion (ω_{1h} and ω_{2h}).

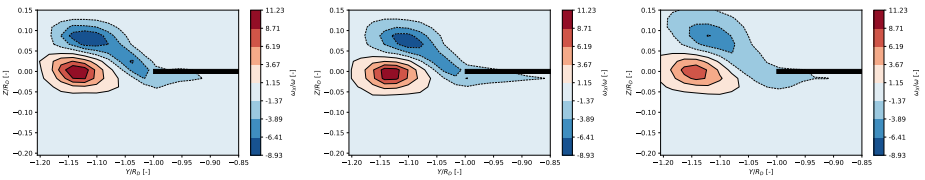

Fig. 15. ω_X/ω_h - YZ radial plane with heave plate (black rectangle) - Case: ω_{1h}, KC_3, λ_1 (left), λ_2 (centre), λ_3 (right), and position $t/T = 0.00$ (zero-down).

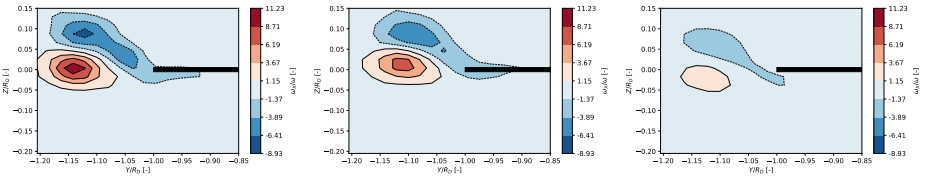

Fig. 16. ω_X/ω_h - YZ radial plane with heave plate (black rectangle) - Case: ω_{2h}, KC_3, λ_1 (left), λ_2 (centre), λ_3 (right), and position $t/T = 0.00$ (zero-down).

In contrast with the velocity magnitude and direction comparison, this analysis reported a higher influence of the scale factor on the magnitude of the minimum and maximum dimensionless vorticity (e.g., averaged increase in maximum dimensionless vorticity of 23.3% between λ_1 and λ_3). This outcome seemed to indicate that the velocity gradients were more affected by scale effects than the velocity vectors. However, this result probably originated from the different spatial resolutions of the recorded images. Lower-resolution images lead to larger smoothing in estimating the velocity derivatives necessary to compute the vorticity. Even though the vorticity was calculated on the same low-resolution grids, the cubic interpolation cannot improve the problem related to the different spatial resolutions of the recorded images (e.g., resolving smaller eddies shedding out from the smaller scale models). Nevertheless, the maximum and minimum vorticity positions appeared to be negligibly affected by the models' dimensions. Furthermore, it was possible to notice small differences in the vorticity field's shape and contours among the three scales.

As similarly carried out for the velocity magnitude, the second investigation was performed by changing only the angular frequency of the heave plate's oscillatory motion and keeping all the other parameters constant (scale ratio included). Figure 15 and Figure 16 show an example of the analysis. This study revealed an increase in minimum and decrease in maximum dimensionless vorticity magnitude for increasing angular frequencies (e.g., averaged increase in maximum dimensionless vorticity of 16.1% for λ_1). This result was expected because of the larger variations in dimensionless velocity magnitude observed for ω_{1h} compared to ω_{2h}. Furthermore, small differences in the vorticity field's centre position among the three models were observed.

It is also relevant to report the maximum and minimum vorticity location as a function of the four positions ($t/T = 0.00$, $t/T = 0.25$, $t/T = 0.50$, and $t/T = 0.75$) and KC (especially to validate numerical models). However, it is impractical to present all the cases: 144 locations for ω_X. A good compromise is to provide the vorticity locations averaged over the three scale ratios (λ_1, λ_2, and λ_3) and the two angular frequencies (ω_{1h} and ω_{2h}). These averaged locations correctly describe the vortex position since the previous investigations revealed a minimal influence of ω and λ on the maximum and minimum vorticity positions. This can also be visually seen by comparing the positions of the maximum and minimum vorticity ($x_\omega^{\max}$ and $x_\omega^{\min}$) with the averaged vorticity locations ($\overline{x_\omega^{\max}}$ and $\overline{x_\omega^{\min}}$) for the previous mentioned cases (KC_3 and position $t/T = 0.00$, zero-down - λ_1, λ_2, and λ_3 - ω_{1h} and ω_{2h}). This comparison, presented in Figure 17, shows the good agreement between the vorticity locations and their averaged values.

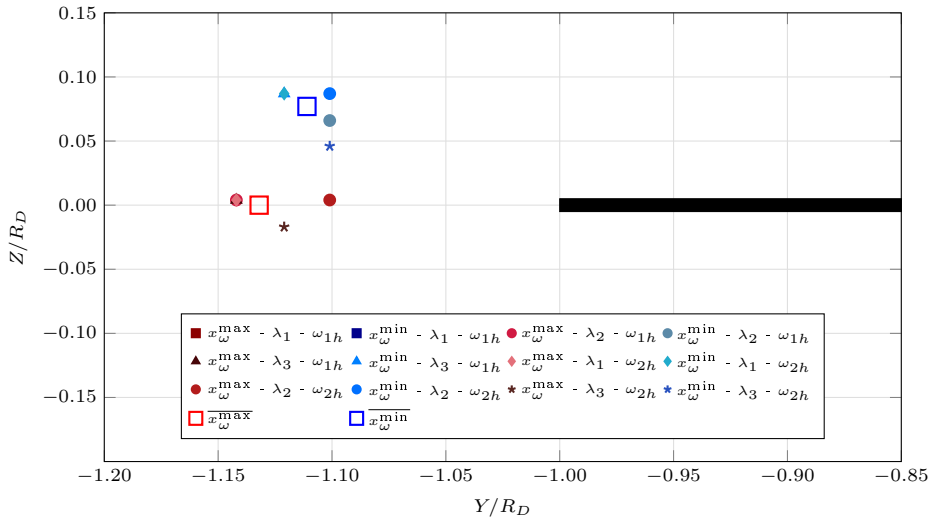

Fig. 17. Location of the maximum and minimum vorticity with heave plate (black rectangle) - Case: ω_{1h}, ω_{2h}, KC_3, λ_1, λ_2, λ_3, and position $t/T = 0.00$ (zero-down).

Based on these considerations, the vorticity locations averaged over the three scale ratios (λ_1, λ_2, and λ_3) and the two angular frequencies (ω_{1h} and ω_{2h}) are displayed in Figures 18-21.

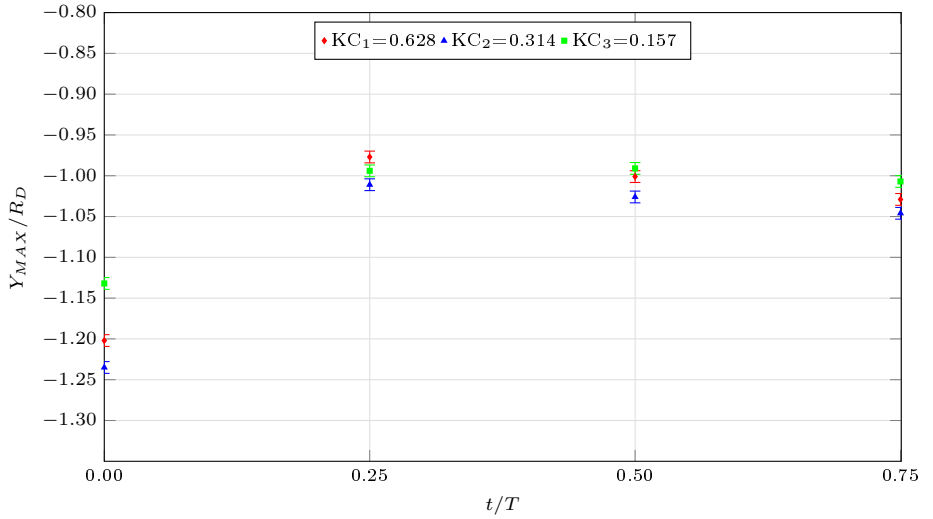

Fig. 18. Horizontal location of the maximum vorticity Y_{MAX} with error bars based on the grid resolution.

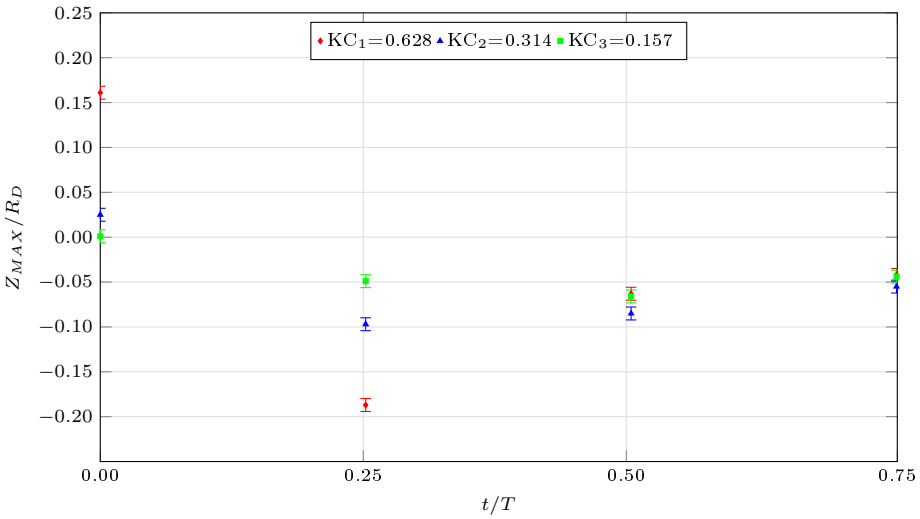

Fig. 19. Vertical location of the maximum vorticity Z_{MAX} with error bars based on the grid resolution.

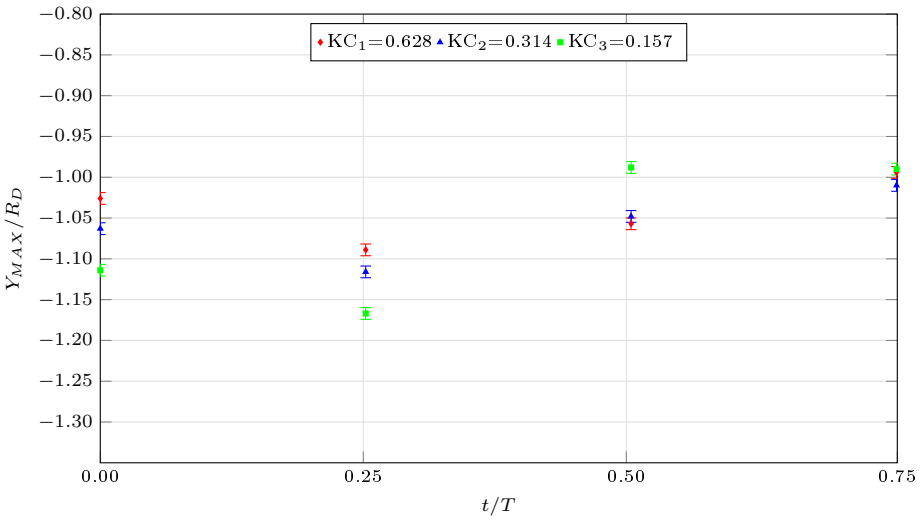

Fig. 20. Horizontal location of the minimum vorticity Y_{MIN} with error bars based on the grid resolution.

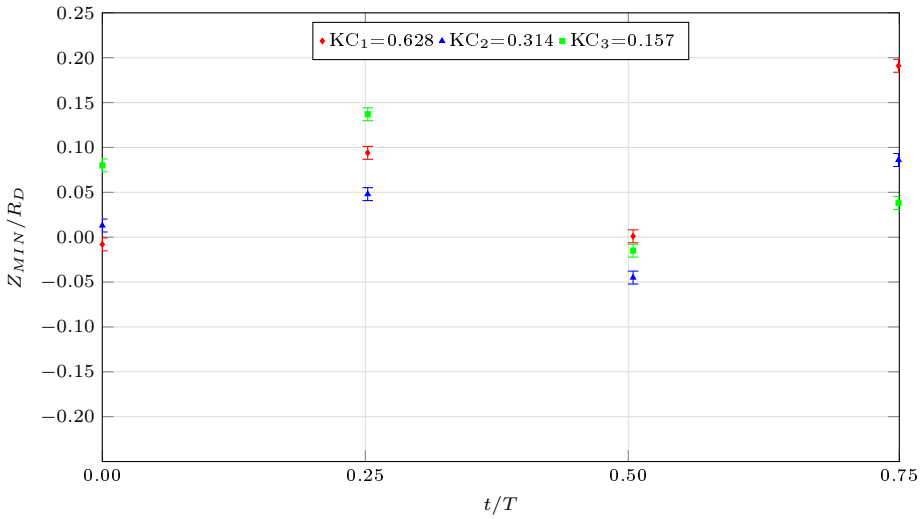

Fig. 21. Vertical location of the minimum vorticity Z_{MIN} with error bars based on the grid resolution.

The reported graphs reveal how KC influences the maximum and minimum locations of the vorticity. For example, for position C ($t/T = 0.25$, bottom), the location of the maximum vorticity was always close to the heave plate. Thus, its horizontal position Y_{MAX}/R_D was close to -1 (see Figure 18) while its vertical position Z_{MAX}/R_D was approximately equal to -0.05 for KC_3, -0.10 for KC_2, and -0.20 for KC_1 (see Figure 19). Similarly, the horizontal location of the minimum vorticity Y_{MIN}/R_D for position A ($t/T = 0.75$, top) was close to -1 (see Figure 20), and its vertical location Z_{MIN}/R_D was close to 0.05 for KC_3, 0.10 for KC_2, and 0.20 for KC_1 (see Figure 21). The variation in minimum vorticity for position A can also be seen in Figure 22. It can be noticed how the minimum vorticity is always near the heave plate, whereas the maximum vorticity location seems to be unaltered by the variation in KC.

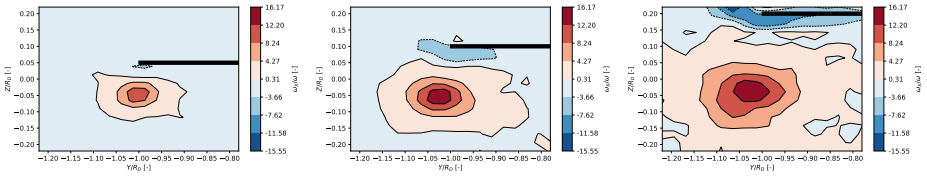

Fig. 22. ω_X/ω_h - YZ radial plane with heave plate (black rectangle) - Case: KC_3 (left), KC_2 (centre), KC_1 (right), ω_{1h}, λ_1, and top position ($t/T = 0.75$).

It is also interesting to compare the vorticity locations between position B (zero position, moving down, $t/T = 0.00$) and D (zero position, moving up, $t/T = 0.50$). Figure 23 show a representative example (ω_{2h}, KC_2, and λ_1) of the two aforementioned positions. It can be noticed the difference in the vorticity field's shape and contours between the two positions. Furthermore, the location of the maximum vorticity appeared to be strongly influenced by the ascending and descending motions of the heave plate (also in terms of vorticity magnitude). This phenomenon was probably

related to the blockage effect caused by the central column.

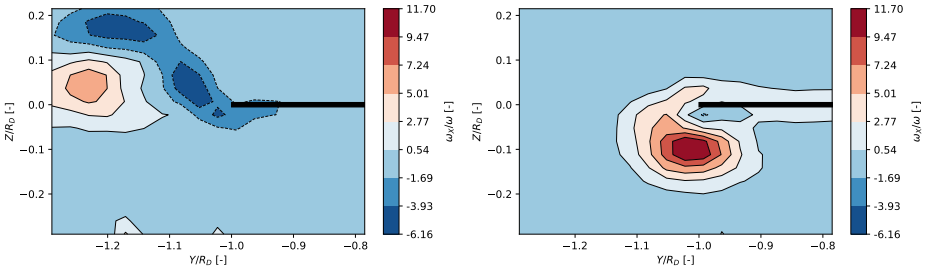

Fig. 23. ω_X/ω_h - YZ radial plane with heave plate (black rectangle) - Case: ω_{2h}, KC_2, λ_1, position $t/T = 0.00$, moving down (left), and position $t/T = 0.50$, moving up (right).

7. Conclusions

The present study summarised the results of forced oscillation flow visualisation model-scale experiments on three geometrically similar one-leg columns of a semi-submersible floating wind turbine platform equipped with a circular solid flat heave plate. The forced oscillation tests were performed at two different frequencies in the range of operational and extreme KCs. The Stereo-PIV images were captured at four positions in the oscillation cycle. Two measurement planes, radial and tangential to the flat heave plate, were captured. The velocity and vorticity fields were analysed and visually examined for all the considered cases, and the main results were reported.

The kinetic energy flow was larger in the radial plane than in the tangential plane, allowing the scale effect analysis to focus on the radial plane. For the radial plane, the out-of-plane velocity component was one order of magnitude lower than the in-plane velocity component. As a result, the velocity field and vorticity analysis was carried out only for the in-plane velocity component.

Similarities in shape, centre positions, and contours between the three different scales were observed for the velocity field. A small increase in the dimensionless velocity magnitude for increasing scale ratios was noticed. The vorticity field also showed similarities in shape, contours, and centre positions among the three different scales. However, in contrast with the velocity comparison, the vorticity investigation revealed a larger influence of the scale factor on the magnitude of the minimum and maximum dimensionless vorticity. Nevertheless, this result was probably caused by the model-scale independent Field of View of the SPIV cameras. Smaller models result in lower resolutions, implying missing some flow details and adding uncertainty in calculating quantities such as vorticity.

The outcomes of this paper confirm the work conducted by Bezunartea-Barrio et al. [16] on the impact of scale effects on the hydrodynamic forces of semi-submersible platforms for the same heave plate models. Two main conclusions can be drawn from the performed research:

1. The selection of a representative KC has a larger influence on the hydrodynamic coefficients than the scale effects caused by the models´ dimensions.
2. The correct estimation of the added damping utilised in numerical simulations (both in frequency and time domain) depends on the selection of a representative motion amplitude (KC).

Furthermore, CFD computations are in progress to compare the velocity and vorticity determined from the SPIV measurements. In future work, once the corresponding literature and technical difficulties are explored in detail, it would also be interesting to compare turbulent flow characteristics (e.g., Reynold's shear stress and turbulent kinetic energy). This was impossible in the current study because the number of recorded images was insufficient to measure turbulent fluctuations correctly [27].

8. Supplementary material

Supplementary data associated with this article can be found at:
http://canal.etsin.upm.es/papers/saettoneetal2022/

CRediT authorship contribution statement

Simone Saettone: Software, Formal analysis, Data Curation, Writing - Original Draft, Writing - Review & Editing, and Visualization. **Enrique Molinelli Fernandez**: Methodology, Investigation, and Writing - Review & Editing. **Cristina Soriano Gómez**: Investigation, and Writing - Review & Editing. **Leandro Antonio Saavedra Ynocente**: Investigation, and Writing - Review & Editing. **Daniel Duque**: Conceptualization, Software, Writing - Review & Editing, and Visualization. **Antonio Souto-Iglesias**: Conceptualization, Methodology, Writing - Review & Editing, Supervision, Project Administration, and Funding acquisition. **Adolfo Maron Loureiro**: Conceptualization, Writing – Review & Editing, Supervision, Project Administration, and Funding acquisition.

Declaration of competing interest

All authors have participated in the conception, analysis, and interpretation of the data, revising the article critically, and approving the final version. The authors have no affiliation with any organization with a direct or indirect financial interest in the subject matter discussed in the manuscript. The authors confirm that this work is original and has not been published elsewhere.

Acknowledgements

The authors want to express their gratitude for the financial support received by the Ministerio de Ciencia e Innovación (MCIU) under Grants RTI2018-096791-B-C21 and RTI2018-096791-B-C22 "Hidrodinámica de elementos de amortiguamiento del movimiento de aerogeneradores flotantes".

References

[1] P. Friedlingstein, M. O'Sullivan, M. W. Jones, R. M Andrew, J. Hauck, A. Olsen, G. P. Peters, W. Peters, J. Pongratz, S. Sitch, et al. Global carbon budget 2020. *Earth System Science Data*, 12(4):3269–3340, 2020.

[2] S. Saettone, B. Taskar, S. Steen, and P. Andersen. The influence of the propeller loading on the thrust deduction fraction. *Ship Technology Research*, pages 1–9, 2021.

[3] S. Saettone, B. Taskar, S. Steen, and P. Andersen. Experimental measurements of propulsive factors in following and head waves. *Applied Ocean Research*, 111: 102639, 2021.

[4] R. Pinguet, S. Kanner, M. Benoit, and B. Molin. Validation of open-source overset

mesh method using free-decay tests of floating offshore wind turbine. In *The 30th International Ocean and Polar Engineering Conference*. OnePetro, 2020.

[5] International Renewable Energy Association et al. Future of Wind: Deployment, Investment, Technology, Grid Integration and Socio-Economic Aspects (A Global Energy Transformation paper). Abu Dhabi: International Renewable Energy Agency, 2019.

[6] R. Pinguet, S. Kanner, M. Benoit, and B. Molin. Modeling the dynamics of freely-floating offshore wind turbine subjected to waves with an open-source overset mesh method. In *International Conference on Offshore Mechanics and Arctic Engineering*, volume 84768, page V001T01A008. American Society of Mechanical Engineers, 2021.

[7] N. T. Philip, S. Nallayarasu, and S. K. Bhattacharyya. Experimental investigation and CFD simulation of heave damping effects due to circular plates attached to spar hull. *Ships and Offshore Structures*, 14(4):396–411, 2019.

[8] A. Medina-Manuel, E. Botia-Vera, S. Saettone, J. Calderon-Sanchez, G. Bulian, and A. Souto-Iglesias. Hydrodynamic coefficients from forced and decay heave motion tests of a scaled model of a column of a floating wind turbine equipped with a heave plate. *Ocean Engineering*, 252:110985, 2022.

[9] K. P. Thiagarajan. *Hydrodynamics of oscillating cylinders and disks at low Keulegan-Carpenter numbers*. PhD thesis, The University of Michigan, 1993.

[10] H. He, A. W. Troesch, and M. Perlin. Hydrodynamics of damping plates at small KC numbers. In *IUTAM symposium on fluid-structure interaction in ocean engineering*, pages 93–104. Springer, 2007.

[11] J. N. Fernando and D. E. Rival. On vortex evolution in the wake of axisymmetric and non-axisymmetric low-aspect-ratio accelerating plates. *Physics of Fluids*, 28 (1):017102, 2016.

[12] J. N. Fernando and D. E. Rival. Reynolds-number scaling of vortex pinch-off on low-aspect-ratio propulsors. *Journal of Fluid Mechanics*, 799, 2016.

[13] S. Satheesh and F. J. Huera-Huarte. Effect of free surface on a flat plate translating normal to the flow. *Ocean Engineering*, 171:458–468, 2019.

[14] X.l. Tian, J. M. Yang, X. Li, and Y. G. Shen. Effects of Reynolds Number on the Hydrodynamic Characteristics of Heave Damping Plate. *Journal of Ship Mechanics*, 17(12), 2013.

[15] E. Anglada-Revenga, A. Bezunartea-Barrio, A. Maron-Loureiro, E. Molinelli-Fernandez, J. Oria-Escudero, L. Saavedra-Ynocente, C. Soriano-Gomez, D. Duque-Campayo, J. Gomez-Goni, and A. Souto-Iglesias. Scale Effects in Heave Plates: PIV Investigation. In *International Conference on Offshore Mechanics and Arctic Engineering*, volume 84416, page V009T09A061. American Society of Mechanical Engineers, 2020.

[16] A. Bezunartea-Barrio, S. Fernandez-Ruano, A. Maron-Loureiro, E. Molinelli-Fernandez, F. Moreno-Buron, J. Oria-Escudero, J. Rios-Tubio, C. Soriano-Gomez, A. Valea-Peces, C. Lopez-Pavon, et al. Scale effects on heave plates for semi-submersible floating offshore wind turbines: case study with a solid plain plate. *Journal of Offshore Mechanics and Arctic Engineering*, 142(3), 2020.

[17] A. Cordle, J. Jonkman, et al. State of the art in floating wind turbine design tools. In *The twenty-first international offshore and polar engineering conference*. International Society of Offshore and Polar Engineers, 2011.

[18] A. N. Simos, F. Ruggeri, R. A Watai, A. Souto-Iglesias, and C. Lopez-Pavon. Slow-drift of a floating wind turbine: An assessment of frequency-domain methods based on model tests. *Renewable energy*, 116:133–154, 2018.

[19] C. Lopez-Pavon, R. A. Watai, F. Ruggeri, Alexandre N. Simos, and A. Souto-Iglesias. Influence of wave induced second-order forces in semisubmersible fowt mooring design. *Journal of Offshore Mechanics and Arctic Engineering*, 137(3), 2015.

[20] M. Frémond, F. Maceri, and G. Vairo. *Models, Simulation, and Experimental Issues in Structural Mechanics*. Springer, 2017.

[21] T. Sarpkaya, M. Isaacson, and J. V. Wehausen. Mechanics of wave forces on offshore structures. 1982.

[22] L. Tao, B. Molin, Y. M. Scolan, and K. Thiagarajan. Spacing effects on hydrodynamics of heave plates on offshore structures. *Journal of Fluids and structures*, 23(8):1119–1136, 2007.

[23] C. Audoly, T. Gaggero, E. Baudin, T. Folegot, E. Rizzuto, R. Salinas Mullor, M. André, C. Rousset, and P. Kellett. Mitigation of underwater radiated noise related to shipping and its impact on marine life: A practical approach developed in the scope of aquo project. *IEEE Journal of Oceanic Engineering*, 42(2):373–387, 2017.

[24] M. Raffel, C. E Willert, F. Scarano, C. J. Kähler, S. T. Wereley, and J. Kompenhans. *Particle image velocimetry: a practical guide*. Springer, 2018.

[25] F. G. Ergin. Dynamic masking techniques for particle image velocimetry. *Isı Bilimi ve Tekniği Dergisi*, 37(2):61–74, 2017.

[26] C. A. Garrido-Mendoza, K. P. Thiagarajan, A. Souto-Iglesias, A. Colagrossi, and B. Bouscasse. Computation of flow features and hydrodynamic coefficients around heave plates oscillating near a seabed. *Journal of Fluids and Structures*, 59:406–431, 2015.

[27] G. Avallone, F. De Gregorio, and G. P. Romano. PIV measurements of turbulence decay behind a grid. In *Particle Image Velocimetry: Recent Improvements*, pages 263–277. Springer, 2004.